Characterizing Multi-Subevent Earthquakes Using the Brune Source Model

Meichen Liu[1], Yihe Huang[1], and Jeroen Ritsema[1]

[1]Department of Earth and Environmental Sciences, University of Michigan, Ann Arbor, MI, USA.

Corresponding author: M. Liu (meichenl@umich.edu)

Key Points:

- We use global source time functions to investigate the Brune source parameters of multi-subevent earthquakes
- We find that the master event corner frequencies correlate better with those of the large subevent
- The Brune stress drop is better correlated with the stress change of the asperity with the largest moment release

Abstract

Although the Brune source model describes earthquake moment release as a single pulse, it is widely used in studies of complex earthquakes with multiple episodes of high moment release (i.e., multiple subevents). In this study, we investigate how corner frequency estimates of earthquakes with multiple subevents are biased if they are based on the Brune source model. By assuming complex sources as a sum of multiple Brune sources, we analyze 1,640 source time functions (STFs) of Mw 5.5-8.0 earthquakes in the SCARDEC catalog to estimate the corner frequencies, onset times, and seismic moments of subevents. We identify more subevents for strike-slip earthquakes than dip-slip earthquakes, and the number of resolvable subevents increases with magnitude. We find that earthquake corner frequency correlates best with the corner frequency of the subevent with the highest moment release (i.e., the largest subsevent). This suggests that, when the Brune model is used, the estimated corner frequency and therefore the stress drop of a complex earthquake is determined primarily by the largest subevent rather than the total rupture area. Our results imply that the stress variation of asperities, rather than the average stress change of the whole fault, contributes to the large variance of stress drop estimates.

Plain Language Summary

The Brune source model, which describes earthquakes as a single pulse of energy release with time, is widely used to study earthquake sources regardless of the true source process. However, multiple energy-release pulses, termed subevents for an earthquake, are not uncommon. The Brune source is characterized by its corner frequency that is related to the inverse of source duration. The frequency spectrum begins to decay at the corner frequency, thereby controlling the hazardous high-frequency ground motions. In this study, we explore the relationship between the corner frequency of an earthquake and corner frequencies of its subevents. Assuming each subevent is a Brune source, we extract corner frequencies of subevents for 1,640 earthquakes recorded in a global dataset, and find the earthquake corner frequency is closely related to the corner frequency of the subevent with the highest energy release. It indicates that the stress release converted from the Brune-source corner frequency of an earthquake represents the stress release in the source region of its largest subevent rather than of the entire earthquake. Our findings improve interpretation of the corner frequency obtained from the Brune source model and help explain the large uncertainty of stress release estimates.

1 Introduction

The classical earthquake source model proposed by J. Brune more than five decades ago (Brune, 1970) is still widely used to understand the initiation of faulting, the propagation of a fault rupture, and the radiation of seismic energy. In the Brune model, a circular crack instantaneously experiences a shear dislocation due to a constant stress drop (i.e., the change of stress) on the fault. The Brune model links three key elements of an earthquake: the seismic moment, corner frequency, and stress drop with simple functions in which the seismic moment and corner frequency are the two free parameters. The Brune model predicts that the source spectrum is constant at frequencies lower than the corner frequency, and decays proportional to the square of frequency at frequencies higher than the corner frequency, an important feature for the calculation of high-frequency ground motions for engineering applications (Papageorgiou and Aki, 1983; Purvance and Anderson, 2003; Sotiriadis et al., 2021). Numerous studies of small and large, shallow and deep, tectonic and induced earthquakes using regional and teleseismic data are based on the Brune source model when estimating stress drops (e.g., Abercrombie, 1995; Garcia et al., 2004; Allmann & Shearer, 2009; Baltay et al., 2011; Oth, 2013; Chen & Shearer, 2018; Huang et al., 2016; Ruhl et al., 2017; Prieto et al., 2017; Trugman et al., 2017; Wu et al., 2018; Shearer et al., 2019; Liu et al., 2020; Yu et al., 2021).

Nevertheless, it is well recognized that earthquakes are complex on a wide variety of spatial and temporal scales. The barrier (Das and Aki, 1977) and asperity (Lay and Kanamori, 1981; Lay et al., 1982) models describe stress and frictional differences on the fault plane. The rupture velocity and the moment rate during rupture expansion can change due to dynamic waves in fault damage zones (e.g., Huang and Ampuero, 2011) as well as fault curvature and segmentation (e.g., Ando and Kaneko, 2018; Ulrich et al., 2019). The complexity of rupture processes is evident for Mw > 7 earthquakes (e.g., Ye et al. 2016; Hayes, 2017) but also for smaller earthquakes (e.g., Boatwright, 1984). Using local seismic arrays, moment rate fluctuations have been observed for Mw < 3.5 earthquakes in the Charlevoix, Quebec seismic zone (Li et al., 1995; Fischer, 2005), on the San Andreas Fault (Wang et al., 2014; Abercrombie, 2014; Abercrombie et al., 2020), and in the 2008 Mogul, Nevada swarm (Ruhl et al., 2017). Danré et al. (2019) used the Gaussian source model to systematically analyze the source complexity for SCARDEC STFs. They observed increasing source complexity with earthquake and an important scaling of the moment of subevent with the earthquake moment by a factor of 0.8. For the Brune source model, the source complexity may cause earthquake source spectra to deviate from the frequency-squared spectral decay for moderate to large (e.g., Luco, 1985; Atkinson, 1993; Beresnew and Atkinson, 2001; Denolle and Shearer, 2016; Yin et al., 2021) and small earthquakes (e.g., Uchide and Imanishi, 2016). The Brune source model has also been modified to include two corner frequencies to explain the deviation (Archuleta & Ji, 2016; Denolle and Shearer, 2016; Uchide and Imanishi, 2016; Ji & Archuleta, 2021).

For many earthquakes, however, there are insufficient data to model source complexity. It is also not a common practice to use complex source models to predict earthquake ground

motions. Therefore, the Brune source model is still widely used to estimate source parameters and ground motions regardless of earthquake source complexity. This poses a fundamental question: What is measured by the Brune source model when it is applied to complex earthquakes?

Here we investigate what kind of source properties are represented by the Brune source model for earthquakes with multiple episodes of high moment release (i.e., multiple subevents). We first quantify earthquake source complexity by analyzing the number and source properties of subevents in source time functions (STFs) of hundreds of Mw 5.5 – 8.0 earthquakes in the SCARDEC (Seismic source CHAracteristic Retrieved from DEConvolving teleseismic body waves) catalog (Vallée and Douet, 2016). We describe and decompose the STF as a sum of Brune sources, and estimate corner frequencies and seismic moments of subevents. By comparing measured source complexity to that observed by Danré et al. (2019), we will further understand the scaling relationship between the source complexity and the subevent moment. We also derive the theoretical source spectrum of a complex earthquake with two Brune subevents. Using both SCARDEC analysis and theoretical derivation, we compare the earthquake's overall corner frequency to the corner frequencies of individual subevents, and show how earthquake corner frequency and stress drop depend on the temporal spacing and relative moments of subevents.

2 Methods

2.1 Source Time Function decomposition

In the time domain, the Brune source is defined as

$$\Omega(t, t_0, f_c, M_0) = M_0(2\pi f_c)^2(t - t_0)e^{-2\pi f_c(t-t_0)}H(t - t_0) \quad (1)$$

where $H(t - t_0)$ is the Heaviside function, t_0 is the onset time of the rupture, M_0 is the seismic moment, and f_c is the corner frequency that is scaled to a characteristic rupture time 1 / f_c. The Brune model predicts a far-field spectrum

$$\Omega(f, f_c, M_0) = \frac{M_0}{1 + \frac{f^2}{f_c^2}} \quad (2)$$

which has a plateau at frequencies much lower than f_c and decreases proportional to f^2 at frequencies higher than f_c. The stress drop $\Delta\sigma$ is proportional to f_c^3 (Madariaga, 1976).

We call the Brune source that best matches the STF of an earthquake Ω_{STF}. The seismic moment and corner frequency of Ω_{STF} are M_{STF} and f_{STF}, respectively. To determine M_{STF} and f_{STF} we transform the SCARDEC STF to the frequency domain using a Fast Fourier Transform algorithm (Cooley and Tukey, 1965) and estimate f_{STF} in the frequency range of 0.01 – 2.0 Hz using the trust-region-reflective least-square algorithm (Branch et al., 1999). For a complex STF with multiple maxima, M_{STF} approximates the earthquake's integrated moment rate, and f_{STF} represents an average value of the rupture duration.

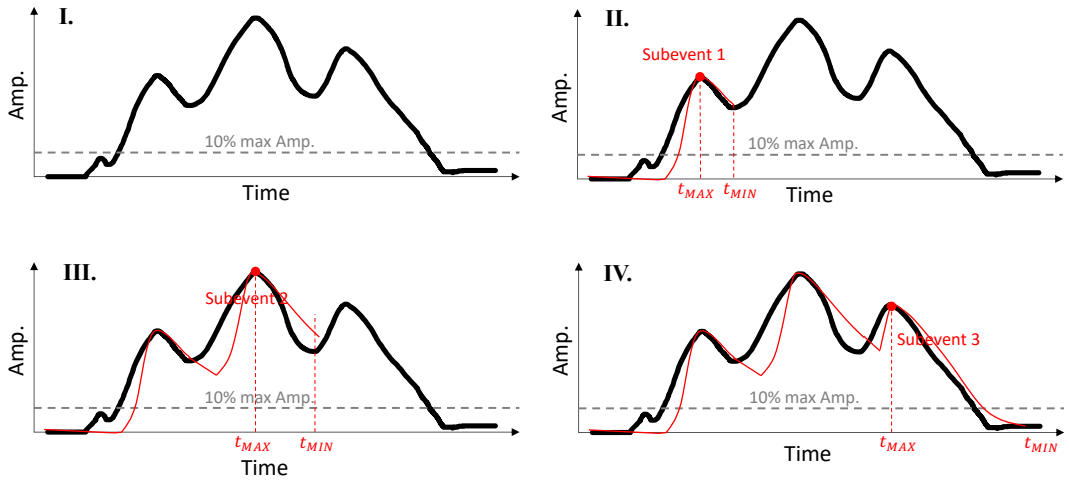

Figure 1. Flowchart of STF decomposition that finds the best corner frequency of subevents that minimizes the misfit one by one in time series. See main text for detailed processes to locate subevents and fit corner frequencies.

To model a complex STF with multiple episodes of high moment rate (i.e., multiple subevents), we write the STF as a sum of Brune pulses:

$$\Omega_{SUM}(t) = \sum_{N=1}^{N_{ev}} \Omega_N(t, t_N, f_N, M_N) \quad (3)$$

To determine the number of resolvable Brune pulses in Ω_{SUM}, we follow the iterative approach by Danré et al. (2019) with some modifications (Figure 1). There are three essential steps: i) To determine subevent *N*, find the time t_{MAX} of the *N* local maximum in the STF that is larger than 10% of the STF's maximum value to avoid overfitting small oscillations as individual subevents. Then we find the time t_{MIN} of the first local minimum in the STF more than 0.5 s after t_{MAX}, to avoid overfitting oscillations close to each other as individual subevents. This requirement should not affect the number of subevents because 0.5 s is only about 10% and 1% of the rupture duration of M5.5 and M8 earthquakes. Ii) Find the seismic moment M_N and corner frequency f_N of subevent *N* that minimize the least-squares difference between the STF and $\Omega_{SUM} = \sum_{k=1}^{N} \Omega_k(t, t_k, f_k, M_k)$ in the time range $[0, t_{MIN}]$. Iii) Repeat steps i) and ii) gradually adding subevents to Ω_{SUM} until the last subevent N_{ev}. We normalize the STFs such that the total integrated area is 1.0 and calculated the residual curve between the STF and Ω_{SUM}. We then calculated the integrated area of the residual curve to obtain the misfit. We discard STFs if the misfit is larger than 0.5. Analogous to the estimate of M_{STF} and f_{STF} we define M_{SUM} and f_{SUM} as the seismic moment and corner frequency of a single Brune pulse that best matches Ω_{SUM} in a least-squares sense.

2.2 Source Time Functions as a sum of two Brune pulses

We derive for the first time the source time functions and source spectra of earthquakes with multiple subevents whose spectra are described by the Brune model. We focus on

earthquakes with two subevents. As shown in section 3.2, two-subevents earthquakes account for 43% of the SCARDEC dataset. The expression of source time functions can also be extended to earthquakes with three or more subevents. We write the source time function of an earthquake with two subevents as

$$\Omega_{SUM}(t) = \Omega_L(t, t_L, f_L, M_L) + \Omega_S(t, t_S, f_S, M_S) \quad (4)$$

where the parameters t_L, f_L, and M_L and the parameters t_S, f_S, and M_S are the onset times, corner frequencies, and seismic moments of the large and small subevents Ω_L and Ω_S, respectively. The power spectrum of Ω_{SUM} for two pulses is

$$\Omega^2_{SUM}(f) = \frac{M_L^2}{k_L^2} + \frac{M_S^2}{k_S^2} + \frac{2M_S M_L}{k_S k_L}\cos\{2\pi f(t_L - t_S) + \alpha_L - \alpha_S\} \quad (5)$$

where $k_L = 1 + f^2/f_L^2$, $k_S = 1 + f^2/f_S^2$, $\sin^2\alpha_L = (k_L - 1)/k_L$, and $\sin^2\alpha_S = (k_S - 1)/k_S$. The first and second terms in (5) are Brune spectra with different low-frequency plateaus and corner frequencies that determine the onset of the spectral fall off. The third term represents oscillations in the spectrum with periods determined by T and the phase shifts determined by f_L and f_S. We reduce the number of free parameters to four by considering the moment ratio $M = M_L/M_S$ and the onset time difference $T = t_L - t_S$ of the largest and smallest subevents instead of M_L, M_S, t_L, and t_S individually.

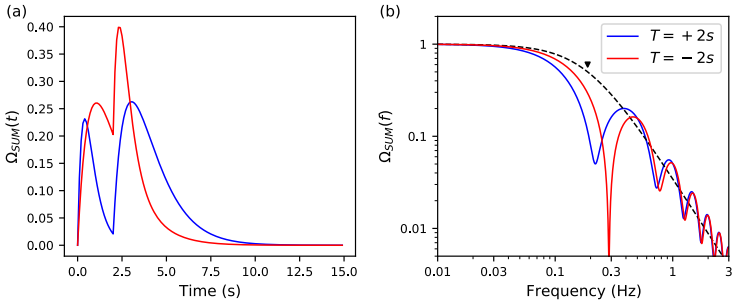

Figure 2. (a) Ω_{SUM} for a sum of two Brune pulses. The large and small subevents have corner frequencies of 0.15 Hz and 0.40 Hz, respectively. The moment ratio $M = M_L/M_S = 3$. In cases 1 (red) and 2 (blue), the largest pulse is the first and second in the sequence so T = -2 s and T = +2 s, respectively. (b) Amplitude spectra (solid lines) of the STFs with corresponding colors shown in (a). The dashed line is the spectrum of a single-pulse Brune source that best matches Ω_{SUM} in a least-squares sense. They are virtually the same for T = -2 s and T = +2 s. The corner frequency of this Brune source is f_{SUM} = 0.19 Hz.

Figure 2 illustrates the typical form of Ω_{SUM} in the time (Figure 2a) and frequency (Figure 2b) domains. Ω_{SUM} has two subevents with corner frequencies f_L = 0.15 Hz and f_S = 0.40 Hz and a moment ratio M = 3. We consider T = -2 s and T = +2 s for which the large subevent precedes and succeeds the small subevent by two seconds, respectively (Figure 2a). The order of the small and the large subevent can significantly change the shape of the STF and its peak values. For example, when T = -2 s, the two maxima in the STF are similar but for T = +2 s, the second maximum is 60% higher than the first one. The spectra for T = -2 s and T = +2 s have

local minima at different frequencies, and they converge and decay approximately proportional to f^2 at frequencies higher than about 0.5 Hz (Figure 2b). The Brune pulse that optimally fits Ω_{SUM} has a corner frequency f_{SUM} = 0.19 Hz for both T = -2 s and T = +2 s, about two times lower than f_S. The location of the first spectral minimum and the spectral decay at high frequencies depend on the values of f_L, f_S, M, and T.

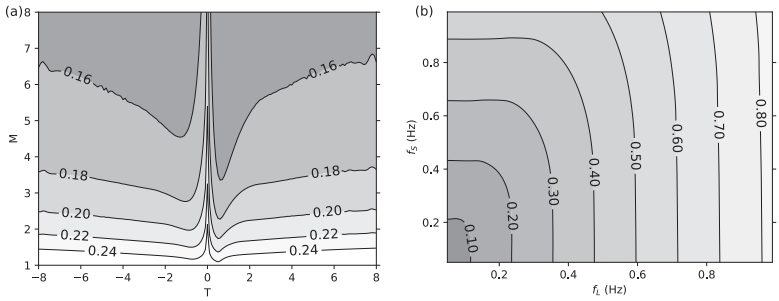

Figure 3. (a) Contour plot of the corner frequency f_{SUM} as a function of T and M. The subevent corner frequencies are f_L = 0.15 Hz and f_S = 0.40 Hz. (b) Contour plot of f_{SUM} as a function of f_L and f_S. The moment ratio and onset time difference of the two subevents are T = 2 s and M = 3.

Figure 3a shows how f_{SUM} varies as a function of T and M for ranges we resolve for the majority of STFs in the SCARDEC catalog with two subevents. As in Figure 2, f_L is 0.15 Hz and f_S is 0.40 Hz. For high values of M, f_{SUM} approaches f_L because the largest of the two subevents dominates Ω_{SUM}. For values of M near 1 and for T near 0, f_{SUM} is intermediate between f_L and f_S. The asymmetry of f_{SUM} about T = 0 indicates that f_{SUM} depends on the order of the large and small subevents in the STF, especially when the onset time difference between the subevents is small. The asymmetry originates from a phase shift of $2(\alpha_L - \alpha_S)$ when the sign of T changes (see (5)), which is the strongest when M is high. Figure 3b shows how f_{SUM} varies with subevent corner frequencies f_L and f_S. We find that f_{SUM} is more related to f_L than f_S when M = 3 and T = 2. f_{SUM} is closer to the smaller one of f_L and f_S and increases with either of them.

3 Analysis

3.1 The SCARDEC catalog

The SCARDEC catalog with source information of hundreds of earthquakes facilitates our exploration. Although it does not include constraints on fault slip distribution such as the finite-fault modeling databases developed by Ye et al. (2016) and Hayes (2017), it is an order of magnitude larger. The SCARDEC analysis is based on the analysis of the waveforms of the teleseismic body-wave phases P, PcP, PP, ScS, and SH and their surface reflected phases to maximize the range of wave take-off angles in the analysis and thus resolution. There are no simplifications regarding the spatial-temporal complexity of the rupture process, so differences of the STFs at different stations may capture rupture directivity. However, we use the average of the STFs from all stations as an estimate of the overall time dependence of moment rate. The SCARDEC catalog has been used in determining the variations of strain drop, stress drop, and

radiated energy with depth, magnitude, and tectonic settings (Vallée, 2013; Courboulex et al., 2016; Chounet & Vallée, 2018; Denolle, 2018; Yin et al., 2021), as well as inversions for rupture velocity and rupture direction (Chounet et al., 2018).

We decompose STFs of Mw 5.5–8.0 earthquakes between 1992–2017 in the SCARDEC catalog. Out of 3,348 earthquakes, 1,640 earthquakes (49%) have two or more subevents. Danré et al. (2019) identified a higher percentage of earthquakes with multiple subevents (81%) most likely because the Gaussian model describes the source with three free parameters in contrast to the two free parameters in the Brune model. Nevertheless, both studies indicate that at least half of moderate to large earthquakes are complex.

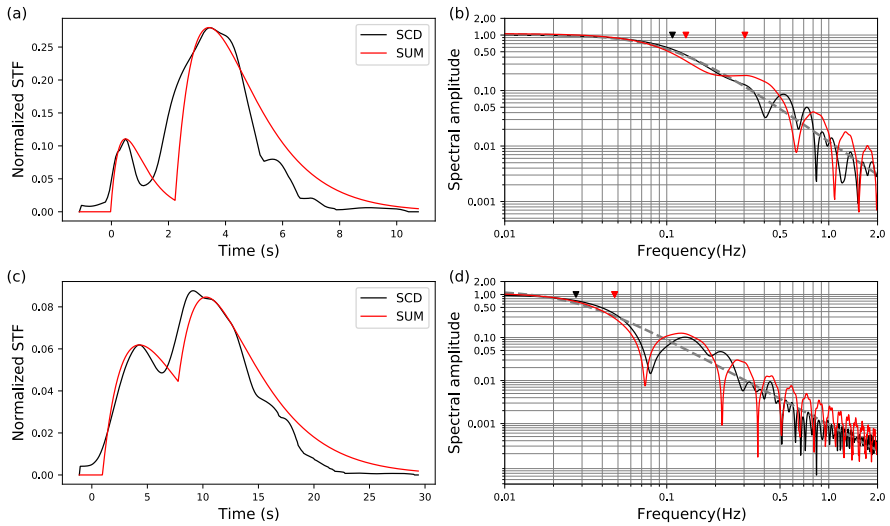

Figure 4. (a) Normalized STFs of the Caroline Islands Mw 6.2 earthquake on December 8, 2017 from the SCARDEC dataset (black line) and the best-fitting sum Ω_{SUM} of two Brune subevents (red line). (b) The spectra of the STF (black line), Ω_{STF} (dashed line) and Ω_{SUM} (red line). The corner frequency f_{STF} = 0.11 Hz is marked by a black reversed triangle. The corner frequencies f_L = 0.13 Hz and f_S = 0.30 Hz are marked by red reversed triangles. (c) and (d) are the same as (a) and (b) but for the southern Chile Mw 7.6 earthquake on December 25, 2016, with corner frequencies f_{STF} = 0.028 Hz, f_L = 0.048 Hz, and f_S = 0.048 Hz and M = 1.08.

As an example, Figures 4a and 4c shows the reconstructed STFs (i.e., Ω_{SUM}) and the original STFs of the December 8, 2017 Mw 6.2 earthquake in Caroline Islands and of the December 25, 2016 Mw 7.6 earthquake in southern Chile. Figures 4b and 4d show their spectra Ω_{STF} and Ω_{SUM}. For the Caroline Islands earthquake, we determine that Ω_{SUM} is a sum of two Brune sources with a moment ratio of 5.75 and with corner frequencies of 0.13 Hz (f_L) and 0.30 Hz (f_S). The large subevent occurred 2.3 seconds after the small subevent. The misfit between the normalized STF and Ω_{SUM} is 32.8%. The corner frequency is inferred to be 0.11 Hz, slightly lower than f_L, because the largest subevent represents more than 85% of the total moment. The observed and synthetic STFs release 90% of the total moment at 6.6 s and 7.8 s. The southern Chile earthquake is also decomposed into two Brune sources although it has a longer source

duration. For this event, the onset time difference T = +6.82 s, and the moment ratio M = 1.08 with a misfit of 18.7%. The corner frequencies f_L and f_S are both 0.048 Hz and much larger than the inferred earthquake corner frequency (0.028 Hz) because the two subevents have similar moments. The observed and synthetic STFs release 90% of the total moment at 17.0 s and 19.3 s, respectively. We note that the synthetic source duration is larger than the observed source duration since the fixed Brune STF decreases slower than the observed STF. Compared to Figure 4d, spectra in Figure 4b have an extra plateau at 0.2 – 0.3 Hz because of the large difference between f_L and f_S.

3.2 Analysis of SCARDEC source time functions

Figure 5 summarizes how the number of subevents varies with moment magnitude, focal mechanism, and source depth. It suggests that the number of subevents increases with moment magnitude in the range of 5.5–8.0 (Figure 5a) and that strike-slip earthquakes are more complex than dip-slip earthquakes (Figure 5b). Earthquakes that have 8 or more subevents are all strike-slip earthquakes. This is in agreement with the previous study by Danré et al. (2019), indicating that the correlation of source complexity with magnitude and faulting type, as quantified by the number of subevents, is a robust characteristic of the SCARDEC catalog and weakly influenced by the assumed source model for the subevent. We also find that shallow (< 50 km) and very deep (> 600 km) earthquakes have more subevents than earthquakes between 50 and 600 km depth (Figure 5c). Patterns in Figure 5b and 5c are also observed in Yin et al. (2021).

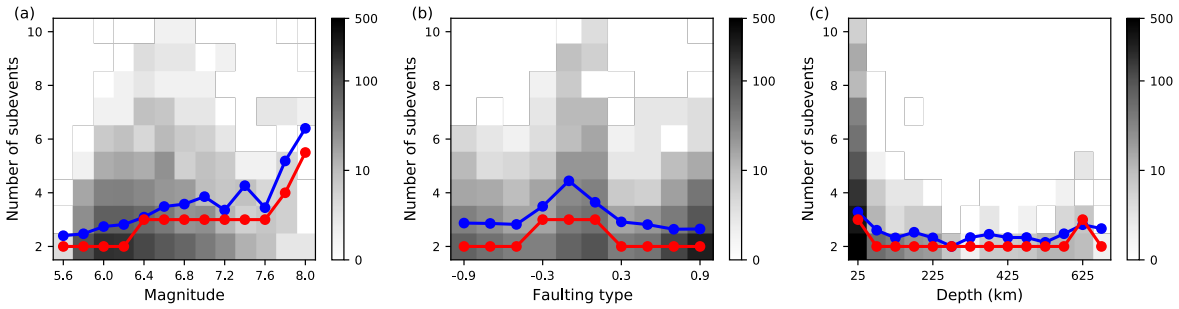

Figure 5. Contour plot of the number of earthquakes. The y-axis shows the number of subevents in the STF up to 10. The x-axis indicates the earthquake's moment magnitude (a), faulting type (b), and focal depth (c). The values of faulting type range from -1 (normal faulting) to 0 (strike-slip faulting) to +1 (reverse faulting) following the quantification by Shearer et al., (2006). Blue and red circles signify means and medians determined for bins of ±0.1 (moment magnitude), ±0.1 (faulting type), and ±25 km (focal depth).

3.3 Analysis of source time functions with two subevents

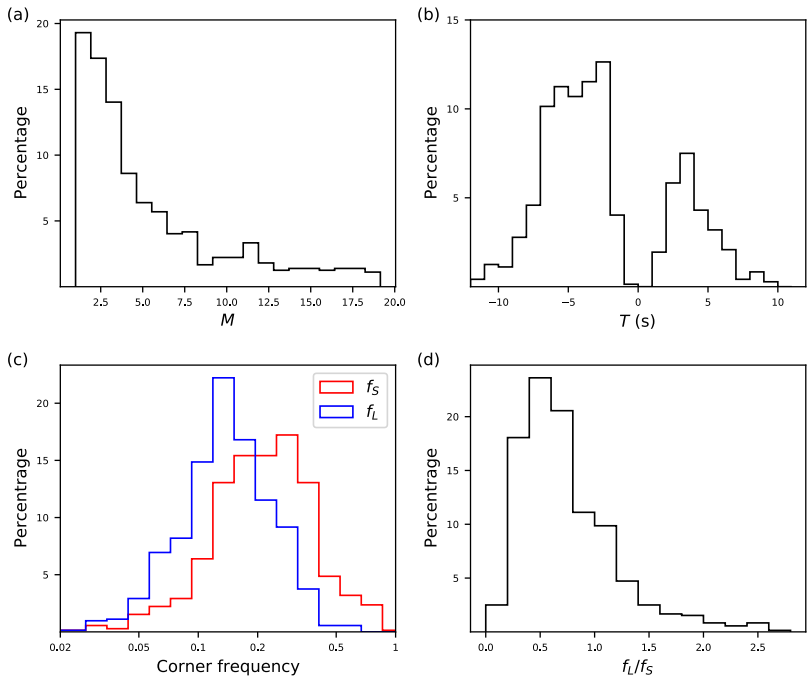

Figure 6. Histograms of (a) moment ratio $M = M_L/M_S$, (b) onset time difference $T = t_L - t_S$, (c) corner frequency of the largest subevent f_L and of the smallest subevent f_S (d) ratio of f_L to f_S for 714 STFs with two subevents in the SCARDEC catalog.

From the 1,640 multi-subevent STFs in the SCARDEC catalog, 714 STFs (43%) have two subevents, more than the sum of the number of earthquakes with three (361), four (198), and five (104) subevents. Since two-subevents earthquakes are most common and the simplest scenario of complex earthquakes, our analysis focuses on earthquakes with two subevents.

The magnitude range of two-subevents earthquakes is Mw 5.7-8.0. The ratio M is lower than 8 for about 75% of the STFs (Figure 6a) and the absolute onset time difference T is between 2.0 and 8.0 s for about 80% of the STFs (Figure 6b). T is negative for 521 STFs, suggesting the largest subevent precedes the smallest subevent more often. The corner frequency f_L of the large subevent has a median value of 0.14 Hz, higher than the corner frequency f_S of the small subevent that has a median of 0.21 Hz (Figure 6c), consistent with the common observation that smaller events have higher corner frequencies. f_L/f_S has a median of 0.65 (Figure 6d), with 76% values smaller than 1.0, which is consistent with the common observation that smaller events tend to have higher corner frequencies.

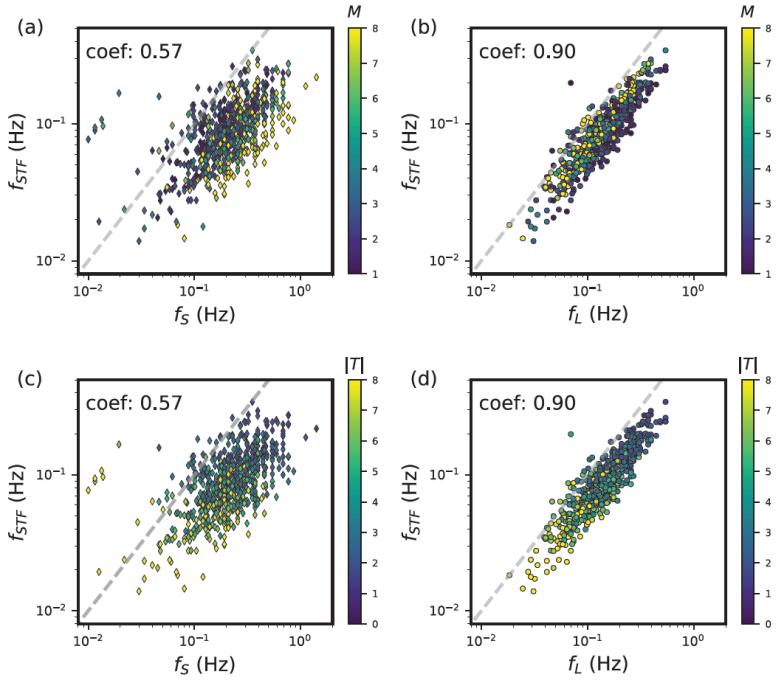

Figure 7. (a) and (b) shows the corner frequency f_{STF} as a function of the corner frequency f_S and f_L color-coded by moment ratio M. (c) and (d) shows the corner frequency f_{STF} as a function of the corner frequency f_S and f_L color-coded by absolute onset time difference $|T|$. The dashed lines indicate a 1:1 correlation.

In Figure 7 we evaluate the significance of the corner frequency f_{STF} of the 714 SCARDEC STFs that are decomposed to have two subevents. The correlation between f_{STF} and f_L (Figures 7b and 7d) is higher than the correlation between f_{STF} and f_S (Figure 7a and 7c) with cross-correlation coefficients of about 0.90 and 0.57, respectively. This indicates that the large subevent determines f_{STF} the most, which agrees with the theoretical results shown in Figure 2b. We find that the corner frequencies of subevents f_S and f_L are overall higher than the earthquake corner frequency f_{STF}. The correlations between f_{STF} and subevent corner frequencies further support the finding of Danré et al. (2019) that the moment of subevents is correlated to the moment of the main event for self-similar earthquakes.

The color-coding in Figures 7a and 7b indicates that with increasing moment ratio M, the difference between f_{STF} and f_S tends to increase while the difference between f_{STF} and f_L tends to decrease, which is also observed in Figure 2a. The plot of the f_S/f_{STF} and f_L/f_{STF} ratios in Figure 8a further illustrate this. The limitation in frequency bandwidth could result in increasing f_S/f_{STF} with M if f_S is high enough, but here most corner frequency estimates are within 0.7 Hz which should be resolvable given a time step of 0.005s. Beginning with a similar spread at M = 1, the scatter in f_S/f_{STF} increases with increasing M, while f_L/f_{STF} tends to cluster to a value of about 1.2. Although f_L/f_{STF} is expected to approach 1 theoretically for the highest values of M, we suspect that the misfit of the decomposition of STF renders Ω_{SUM} to have a slightly different frequency content than Ω_{STF}. Figures 7c and 7d show that for an increasing absolute onset time

difference $|T|$ between subevents, f_{STF} and f_L decreases. This is consistent with the fact that $|T|$ controls the total source duration, which is inversely proportional to the corner frequency of the Brune pulse. Therefore, f_{STF} and the closely correlated f_L, are inversely proportional to $|T|$, whereas the change of f_S with $|T|$ is less obvious due to high scatter.

Figure 8b shows an asymmetry in the ratios f_S/f_{STF} and f_L/f_{STF} with reference to $T = 0$, implying that the order of the large and small subevents of subevent (i.e., $T > 0$ and $T < 0$) has an influence on the corner frequency estimates. The variation in f_S/f_{STF} for $T < 0$ is two times higher than for $T > 0$, suggesting that f_S is similar to f_{STF} and better constrained if the small subevent precedes that large subevent. The variation in ratio f_L/f_{STF} does not change with T, but the mean value of f_L/f_{STF} for $T < 0$ is slightly smaller than f_L/f_{STF} for $T > 0$ (1.60 versus 1.79). Since the absolute value of T is higher than 1 for most STFs in the SCARDEC catalog (see Figure 6b), the relatively small influence of T on f_L/f_{STF} is consistent with Figure 2a, where we found that f_{STF} depends strongly on T only when $|T| < 1$.

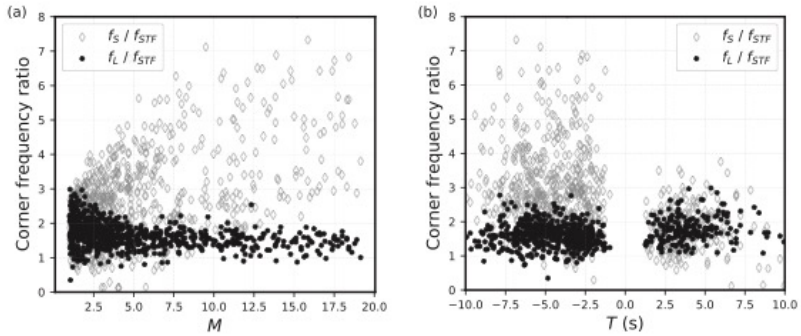

Figure 8. The ratio between corner frequencies f_L (solid black circles) and f_S (gray open diamonds) to f_{STF} as a function of moment ratio M (a) and onset time difference T (b).

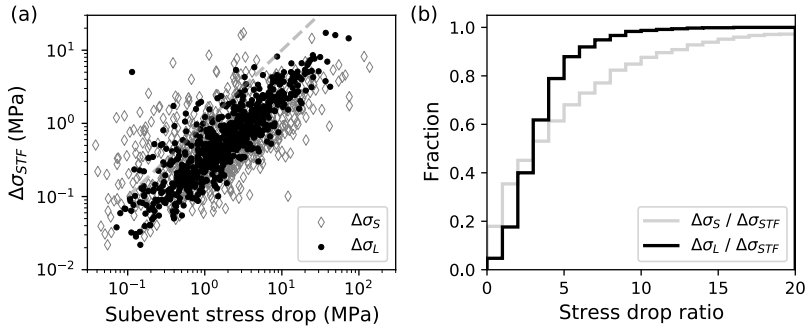

Figure 9. (a) Average stress drop $\Delta\sigma_{STF}$ as a function of the stress drop $\Delta\sigma_L$ (circles) and $\Delta\sigma_S$ (diamonds) of the large and small subevents, respectively. (b) Cumulative fraction of the ratios $\Delta\sigma_L/\Delta\sigma_{STF}$ (black line) and $\Delta\sigma_S/\Delta\sigma_{STF}$ (grey line).

The Brune model relates the corner frequency f_c to stress drop $\Delta\sigma$ assuming a circular crack model:

$$\Delta\sigma = \frac{7M_0 f_c^3}{16\beta^3 k^3} \quad (6)$$

Here k is a constant and β is the shear wave velocity (Madariaga, 1976). In (6), $\Delta\sigma$ represents the average stress change on the fault plane. Analogous to our definitions for f_{STF}, we define $\Delta\sigma_{STF}$ as the average stress drop determined for the SCARDEC STF. Further, we define $\Delta\sigma_L$ and $\Delta\sigma_S$ and M_L and M_S as the stress drops and seismic moments of the large and small subevents, respectively. The shear wave velocity is referred from PREM (Dziewonski & Anderson, 1981) model. We assume the rupture velocity is about 0.7 β (Ye et al., 2016; Hayes, 2017; Chounet et al., 2017). Note that the value of k is related to the spherical average of the corner frequency, and is different for P- and S-waves (Sato & Hirasawa, 1973; Madariaga, 1976; Kaneko & Shearer, 2014, 2015; Wang & Day, 2017). Since SCARDEC STFs are obtained by averaging P and S waves after removal of Green's functions, we set k as 0.32 according to Sato & Hirasawa (2017) and Kaneko & Shearer (2015). $\Delta\sigma_{STF}$, $\Delta\sigma_L$, and $\Delta\sigma_S$ are proportional to the cube of f_{STF}, f_L, and f_S. Therefore, as for f_L, f_S, and f_{STF}, the correlation between $\Delta\sigma_{STF}$ and $\Delta\sigma_L$ is higher than the correlation between $\Delta\sigma_{STF}$ and $\Delta\sigma_S$ (Figure 9a). The correlation of Brune stress drop estimates with the largest asperity supports the usage of the moment-weighted stress drop and the energy-based stress drop (Noda et al., 2013). $\Delta\sigma_L$ and $\Delta\sigma_S$ are also larger than $\Delta\sigma_{STF}$ (Figure 9b). For 50% of the STFs $\Delta\sigma_L$ and $\Delta\sigma_S$ are larger than $\Delta\sigma_{STF}$ by a factor of 4, and stress drops of the small subevents is an order of magnitude higher than the overall stress drop for 20% of the earthquakes in the SCARDEC catalog (see also Figure 6c).

4 Discussion

4.1 Comparison with finite-fault inversion results

Through the STFs decomposition, we find that the corner frequency of the master event is more related to the largest subevent. STFs show temporal behavior of the rupture moment release, however, provide no spatial information of the rupture process. Thus, we compare subevent corner frequencies measured from STFs with rupture dimensions of subevents estimated from finite-fault inversion datasets. Ye et al. (2016) applied finite-fault inversion to teleseismic P waveforms of 114 earthquakes larger than Mw7.0. We fit the source spectra of STFs from finite-fault inversion to the Brune source model to estimate the corner frequency of the earthquake f_{STF} and convert it to rupture radius following $r_{STF} = k\beta/f_{STF}$, where k is a constant and β the shear wave velocity. Assuming an average crustal shear-wave velocity (β = 3.5 km/s), the rupture velocity used by Ye et al. (2016) (2.5 km/s) is 70% of the shear wave velocity. We use corresponding k values of P waves from Sato & Hirasawa (1973) and Kaneko & Shearer (2015). We then decompose STFs to estimate the moment of the largest subevent. Assuming that the largest subevent with the highest slip can be approximated by a circle, we use the moment release distribution to find the radius r_{FNT} when the total moment release within the circle is equal to the largest subevent. As an example, Figures 10a and 10b display the STF for

the 2014 April 18, Guerrero earthquake and its slip map where the circle with a radius of r_{FNT} = 24 km outlines the region of slip of the largest subevent.

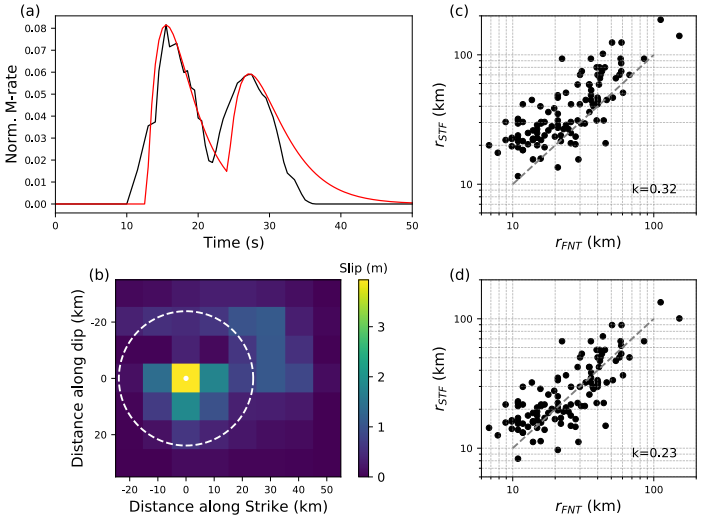

Figure 10. (a) The normalized source time function and (b) slip distribution in Ye et al. (2016) for the April, 18, 2014 Mw7.3 Guerrero earthquake. The black curve in (a) is the STF from finite-fault inversion and the red curve is its decomposition into two Brune sources. The white dashed circle in (b) with a radius r_{FNT} = 24 km signifies the rupture area of the largest subevent. The best-fit Brune corner frequency is f_{STF} = 0.04 Hz. (c) Radius r_{STF} converting from f_{STF} using k = 0.32 as a function of the largest subevent radius r_{FNT} measured from finite-fault inversion. The grey dashed line signifies a 1:1 relation. (d) Same as (c) but with k = 0.23.

Figures 10c and 10d show that r_{STF} are positively correlated with r_{FNT}. The radius r_{STF} depends linearly on k. For k = 0.23 (Sato & Hirasawa, 1973) r_{STF} is about 30% higher than for k = 0.32 (Kaneko & Shearer, 2015), but k has no influence on the correlation between r_{STF} and r_{FNT}. A change of 10% moment would result in approximate 10% change of the radius. We note that the estimation of r_{FNT} is rough because the rupture areas of subevents may not be circles. Nevertheless, the proportionality of r_{STF} and r_{FNT} supports our conclusion that the largest subevent strongly influences estimates of the earthquake corner frequency and rupture dimension, and estimates of earthquake corner frequency represent rupture dimensions of the largest subevent.

4.2 Observed stress drop variability

The stress drops estimated from the SCARDEC STFs dataset have a standard deviation of about a factor of 3.5. This standard deviation is close to the factor-of-three variability of stress drop estimated from the SCARDEC STFs by Courboulex et al. (2016), and is similar to the variability of stress drop estimated from the moment rate functions of earthquakes in dynamic rupture simulations (Gallovic and Valentova, 2020). Allmann and Shearer (2009) obtained a stress drop variability of about a factor of 4.5 using a spectral fitting method based on global eGfs. Our results show that the stress drop variability may be a consequence of earthquake

complexity. Whereas for a simple source, the stress drop inferred from the Brune source corner frequency represents the average stress drop on the fault plane, the stress drop of a complex rupture with multiple subevents is influenced strongly by the largest subevent. Therefore, earthquakes with the same magnitudes can have varying stress drops depending on the source complexity and the largest subevent dimension. This could explain the significant higher variability of stress drop estimated from source time functions of simulated ruptures than the variability of stress drop prescribed in dynamic rupture models (Cotton et al., 2003; Lin and Lapusta, 2018; Gallovic and Valentova, 2020). A better understanding of the source of stress drop variability helps to predict ground velocity and acceleration after major earthquakes, which are essential for the seismic hazard assessment.

We note that, in addition to the source complexity, the simplicity of the Brune source model itself can also lead to a systematic deviation of the stress drop estimation. The Brune source model is widely applied due to its simplicity, but also suffers from inaccurate representation for complex earthquake sources. Although we obtain similar distributions of subevent numbers using the Brune source model as Danré et al. (2019) who used the Gaussian source model, the variation of stress drop estimates is cubed when stress drop is converted from corner frequency estimates. Apart from the model choice, the quality of dataset (Green's function removal in SCARDEC STFs), the frequency bandwidth, and the spectral fit method all contribute to the corner frequency and stress drop variation.

4.3 Application to spectral ratios

Since the spectral ratio method is frequently used to estimate corner frequencies (e.g., Abercrombie, 2015; Huang et al, 2016; Uchide and Imanishi, 2016; Liu et al, 2020) we explore the resolution of the corner frequencies of a large earthquake (referred to as the master event hereafter) after dividing its spectrum Ω_M by the spectrum Ω_E of a co-located but smaller earthquake. The spectral ratio method isolates the source term of the master event, because for the same station the propagation and receiver effects are the same in Ω_M and Ω_E. Therefore, the smaller earthquake can be regarded as the empirical Green's function (referred to as eGf hereafter).

Assuming Brune sources as in eq. (1), the spectral ratio is $\Omega_{RATIO}(f, f_{RATIO}, M_{RATIO}) = \Omega_M(f, f_M, M_M)/\Omega_E(f, f_E, M_E)$, where, M_M, M_E, f_M, f_E are seismic moments and corner frequencies of the master event and the eGf. The spectral ratio Ω_{RATIO} has a seismic moment ratio M_{RATIO} and a first corner frequency f_{RATIO} (i.e., master event corner frequency inferred from the spectral ratio method). Note that the spectral ratio also has a second corner frequency that corresponds to the eGf corner frequency. If f_E is much higher than f_M, Ω_{RATIO} is equivalent to Ω_M and f_M is equivalent to f_{RATIO}. If f_E is similar to f_M, Ω_{RATIO} decays more slowly at high frequencies than Ω_M. There are two approaches to get the source spectral information M_M and f_M: 1) removing the Green's function and performing spectral fitting (e.g., Shearer et al., 2007, 2009), and 2) fitting the spectral ratio of two Brune models based on empirical Green's function

(e.g. Abercrombie, 1995; Abercrombie, 2014, 2015), with two approaches benchmarked in Shearer et al. (2019).

We show the spectra and the spectral ratio of the second spectral ratio approach in Figure 11a. Figures 11c and 11d demonstrate this for the master events used in Figure 2 (i.e., events composed of two subevents with onset time difference of T = -2 s and T = +2 s) that have a corner frequency f_M = 0.19 Hz for both cases of T. The eGfs used to compute Ω_{RATIO} are single-pulse Brune sources with corner frequencies of 0.5 Hz (Figure 11c) and 1.5 Hz (Figure 11d). In both cases, f_{RATIO} is inferred to be lower than f_M because the first oscillation in the spectral ratios causes an earlier and faster decay near f_M (Figure 2b). This decreasing effect on f_{RATIO} is stronger when the eGf has a corner frequency closer to f_M. For f_E higher than 1 Hz, f_{RATIO} approaches f_M asymptotically (Figure 11b). In addition, the sequence of the large and small subevents affects f_{RATIO}. The master event corner frequency is inferred to be larger when large subevent precedes small subevent (T = -2 s).

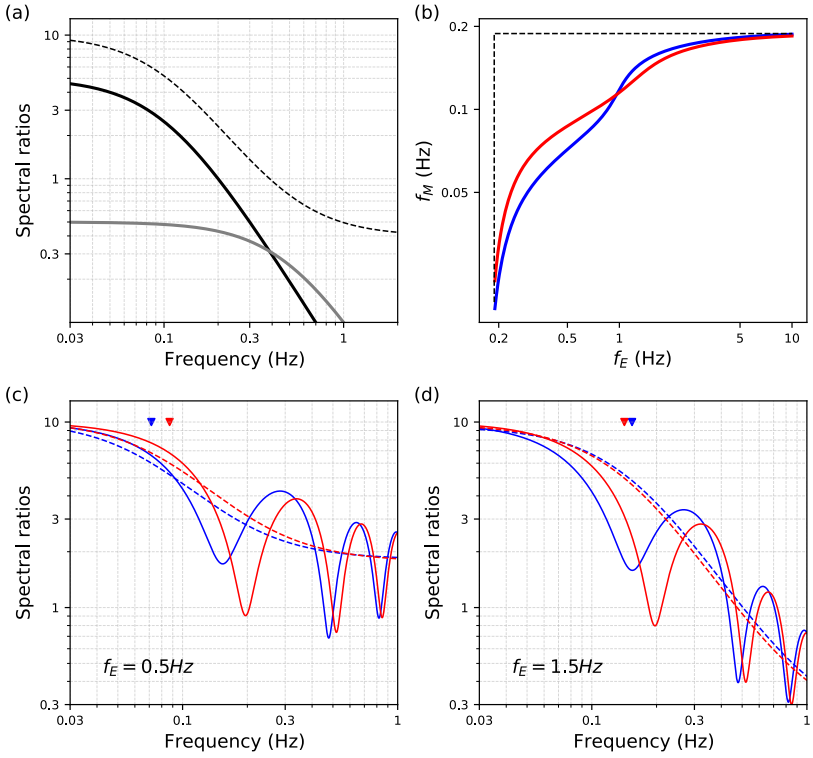

Figure 11. (a) Spectra of the master event (black solid) with f_M = 0.1 Hz, M_M = 5 and the eGf (grey solid) with f_E= 0.5 Hz, M_E = 0.5 Hz as well as their spectral ratio (dashed line). (c) Spectral ratios for T = +2 s (blue) and T = -2 s (red) when f_E = 0.5 Hz. The master event has the same spectra as the spectra shown in Figure 2. The corners f_M of the spectral ratio Ω_M are indicated by reversed triangles for the cases where the large subevent precedes (in red) or succeeds (in blue) the small subevent by 2 s. (d) Same as (a) for f_E = 1.5 Hz. (b) f_M as a function of f_E for T = +2 s (blue) and T = -2 s (red). The horizontal and vertical black dashed lines indicate the corner frequency f_M = 0.19 Hz of the master event.

There is an upper bound of the frequencies (2 Hz in our case) in the source spectrum used for the fitting of the Brune source spectrum. Because Ω_M and Ω_E decay identically above f_E, the first corner of a spectral ratio is primarily determined by signals at frequencies lower than f_E that is usually smaller than the upper frequency range. For multi-subevent earthquakes, oscillations at frequencies smaller than f_E dominate the modeling of spectral ratios. Theoretically, if the eGf has the form of a single-pulse Brune spectrum, its corner frequency does not strongly influence the estimate of the corner frequency of the master event. For complex master events, however, oscillations at frequencies smaller than f_E, rather than the overall fall-off control the fitting. As f_E decreases, we are more likely to fit the first oscillation which has a corner frequency smaller than the master event. Therefore, the spectral ratio method yields a larger variance in the estimated corner frequency than the direct fitting of earthquake source spectra when the master event consists of multiple subevents.

4.4 More complex spectral models

It is necessary to differentiate two subevent corner frequencies in our analysis from the double-corner frequency model (Archuleta and Ji, 2016; Denolle and Shearer, 2016; Uchide and Imanishi, 2016; Wang & Day, 2017; Ji & Archuleta, 2021). The double-corner frequency has an additional corner compared to the Brune source model and variable fall-off rates, so it can better model complex source spectra at high frequency. The underlying physics of an additional corner is an extra time scale relating to one of the following source properties: the slip rise time (Brune, 1970), the time between the starting and stopping phases (Luco, 1985), the spacing of barriers and asperities (Denolle and Shearer, 2016), and the superposition of two subevents (Atkinson, 1993). Our analysis is based on the Brune source model, so we only estimate a single corner frequency of the master event, which characterizes the whole earthquake. Similarly, subevent corner frequencies only characterize the source properties of subevents separately.

4.5 Comparison with previous SCARDEC decomposition results

Our decomposition approach is the same as Danré et al. (2019), but we assume the Brune source instead of the Gaussian source used in their analysis. The Gaussian source model is described by three source parameters and thus more adaptable than the Brune source model with two parameters. Though Danré et al. (2019) resolved more subevents than found in this study, the relative number of subevents per faulting type are consistent in two studies, indicating that source models have no effect on the analysis. Both Danré et al. (2019) and our study showed that the smallest earthquakes have the fewest subevents, but both studies are limited by the decomposition method and the resolvable frequency bandwidth of SCARDEC STFs which are obtained from teleseismic body-wave phases. Because teleseismic waveforms above 0.5 Hz have relatively low signal-to-noise ratios and STFs are averaged over stations, high-frequency contents are deficient in SCARDEC STFs. Additionally, the decomposition method requires subevents to have moments that are at least 10% of the total moment. Therefore, it is likely that smaller subevents were missed by our analysis. The spectral analysis of regional and local seismograms would enable a study of the relationships of corner frequencies and rupture

dimensions of subevents of Mw 3–4 earthquakes to test whether small earthquakes are as complex as large earthquakes (e.g., Fischer, 2005; Abercrombie, 2014, Ruhl et al., 2017).

4.6 Limited frequency range of the SCARDEC STFs

SCARDEC STFs above 0.5 Hz is inaccurate due to the wave attenuation and wave propagation complexities as well as averaging of spectra from global stations. This inherent lack of high frequency of SCARDEC STFs reduces our resolution of subevents for smaller earthquakes, and would lead to a constant resolvable subevent magnitude for different earthquake magnitudes. However, our decomposition results show that the magnitudes of smallest resolvable subevents increase with earthquake magnitude, and the resolvable magnitude range of subevents is almost the same (~1.3) for various earthquake magnitudes (Figure S1), consistent with Danré et al. (2019). It suggests that our decomposition method, which requires a minimum moment rate of subevents according to the STF, controls the resolution of subevents. Therefore, the observed increasing number of subevents with earthquake magnitude is not an artifact.

5 Conclusions

We use SCARDEC source time functions to investigate how estimates of the corner frequency of earthquakes with multiple subevents are biased by assuming a simple Brune source. By decomposing SCARDEC STFs, we find more than half of Mw 5.5–8.0 earthquakes have multiple subevents. We derive theoretical solutions of the source spectrum for an earthquake with two Brune-type subevents. The theoretical derivation demonstrates that the earthquake corner frequency correlates better with the corner frequency of the large subevent than the small subevent. In both synthetic tests and the analysis of the SCARDEC catalog, earthquake corner frequency approaches the largest subevent corner frequency as the moment ratio between subevents increases, whereas the onset time difference between subevents has a minor effect with slight asymmetry. The positive correlation is also observed for earthquake rupture dimension estimated from its corner frequency and rupture dimension of the largest subevent estimated from finite-fault inversion. Our findings suggest that the corner frequency estimates may reflect the stress change of the largest asperity instead of the average stress drop on the whole rupture area, which helps to explain the commonly observed large variance of stress drop estimates.

Acknowledgments, Samples, and Data

This study is sponsored by the National Science Foundation award EAR–2019379. We thank Martin Vallée for advice on the SCARDEC catalog of source time functions. The SCARDEC catalog is available at: http://scardec.projects.sismo.ipgp.fr/. All data and codes used in this paper will be available through Deep Blue Data repository (https://doi.org/10.7302/4ga6-8574).

References

Abercrombie, R. E. (1995). Earthquake source scaling relationships from – 1 to 5 ML using seismograms recorded at 2.5-km depth. *Journal of Geophysical Research: Solid Earth*, *100*(B12), 24015-24036.

Abercrombie, R. E. (2014). Stress drops of repeating earthquakes on the San Andreas fault at Parkfield. *Geophysical Research Letters*, *41*(24), 8784-8791.

Abercrombie, R. E. (2015). Investigating uncertainties in empirical Green's function analysis of earthquake source parameters. *Journal of Geophysical Research: Solid Earth*, *120*(6), 4263-4277.

Abercrombie, R. E., Chen, X., & Zhang, J. (2020). Repeating Earthquakes with Remarkably Repeatable Ruptures on the San Andreas Fault at Parkfield. *Geophysical Research Letters*, *47*(23), e2020GL089820.

Allmann, B. P., & Shearer, P. M. (2009). Global variations of stress drop for moderate to large earthquakes. *Journal of Geophysical Research: Solid Earth*, *114*(B1).

Ando, R., & Kaneko, Y. (2018). Dynamic rupture simulation reproduces spontaneous multifault rupture and arrest during the 2016 Mw 7.9 Kaikoura earthquake. *Geophysical Research Letters*, *45*(23), 12-875.

Archuleta, R. J., & Ji, C. (2016). Moment rate scaling for earthquakes $3.3 \leq M \leq 5.3$ with implications for stress drop. *Geophysical Research Letters*, *43*(23), 12-004.

Atkinson, G. M. (1993). Earthquake source spectra in eastern North America. *Bulletin of the Seismological Society of America*, *83*(6), 1778-1798.

Baltay, A., Ide, S., Prieto, G., & Beroza, G. (2011). Variability in earthquake stress drop and apparent stress. *Geophysical Research Letters, 38*(6).

Beresnev, I., & Atkinson, G. (2001). Subevent structure of large earthquakes—A ground-motion perspective. *Geophysical Research Letters*, *28*(1), 53-56.

Boatwright, J. (1984). The effect of rupture complexity on estimates of source size. *Journal of Geophysical Research: Solid Earth, 89(B2)*, 1132-1146.

Branch, M. A., Coleman, T. F., & Li, Y. (1999). A subspace, interior, and conjugate gradient method for large-scale bound-constrained minimization problems. *SIAM Journal on Scientific Computing*, *21*(1), 1-23.

Chen, X., & Shearer, P. M. (2011). Comprehensive analysis of earthquake source spectra and swarms in the Salton Trough, California. *Journal of Geophysical Research: Solid Earth*, *116*(B9).

Chounet, A., & Vallée, M. (2018). Global and interregion characterization of subduction interface earthquakes derived from source time functions properties. *Journal of Geophysical Research: Solid Earth*, *123*(7), 5831-5852.

Chounet, A., Vallée, M., Causse, M., & Courboulex, F. (2018). Global catalog of earthquake rupture velocities shows anticorrelation between stress drop and rupture velocity. *Tectonophysics*, *733*, 148-158.

Cooley, J. W., & Tukey, J. W. (1965). An algorithm for the machine calculation of complex Fourier series. *Mathematics of computation*, *19*(90), 297-301.

Cotton, F., Archuleta, R., & Causse, M. (2013). What is sigma of the stress drop?. *Seismological Research Letters*, *84*(1), 42-48.

Courboulex, F., Vallée, M., Causse, M., & Chounet, A. (2016). Stress-drop variability of shallow earthquakes extracted from a global database of source time functions. *Seismological Research Letters*, *87*(4), 912-918.

Danré, P., Yin, J., Lipovsky, B. P., & Denolle, M. A. (2019). Earthquakes within earthquakes: Patterns in rupture complexity. *Geophysical Research Letters*, *46*(13), 7352-7360.

Das, S., & Aki, K. (1977). Fault plane with barriers: a versatile earthquake model. *Journal of geophysical research*, *82*(36), 5658-5670.

Denolle, M. A., & Shearer, P. M. (2016). New perspectives on self-similarity for shallow thrust earthquakes. *Journal of Geophysical Research: Solid Earth*, *121*(9), 6533-6565.

Dziewonski, A. M., & Anderson, D. L. (1981). Preliminary reference Earth model. *Physics of the earth and planetary interiors, 25*(4), 297-356.

Fischer, T. (2005). Modelling of multiple events using empirical Green's functions: method, application to swarm earthquakes and implications for their rupture propagation. *Geophysical Journal International*, *163*(3), 991-1005.

Gallovič, F., & Valentová, Ľ. (2020). Earthquake stress drops from dynamic rupture simulations constrained by observed ground motions. *Geophysical Research Letters*, *47*(4), e2019GL085880.

García, D., Singh, S. K., Herráiz, M., Pacheco, J. F., & Ordaz, M. (2004). Inslab earthquakes of central Mexico: Q, source spectra, and stress drop. *Bulletin of the Seismological Society of America, 94*(3), 789-802.

Hayes, G. P. (2017). The finite, kinematic rupture properties of great-sized earthquakes since 1990. *Earth and Planetary Science Letters*, *468*, 94-100.

Huang, Y., & Ampuero, J. P. (2011). Pulse-like ruptures induced by low-velocity fault zones. *Journal of Geophysical Research: Solid Earth*, *116*(B12).

591 Huang, Y., Beroza, G. C., & Ellsworth, W. L. (2016). Stress drop estimates of potentially
592 induced earthquakes in the Guy-Greenbrier sequence. *Journal of Geophysical Research: Solid*
593 *Earth*, *121*(9), 6597-6607.

594 Ji, C., & Archuleta, R. J. (2021). Two Empirical Double-Corner-Frequency Source Spectra and
595 Their Physical Implications. *Bulletin of the Seismological Society of America, 111*(2), 737-761.

596 Kaneko, Y., & Shearer, P. M. (2015). Variability of seismic source spectra, estimated stress
597 drop, and radiated energy, derived from cohesive-zone models of symmetrical and asymmetrical
598 circular and elliptical ruptures. *Journal of Geophysical Research: Solid Earth*, *120*(2), 1053-
599 1079.

600 Lay, T., Kanamori, H., & Ruff, L. (1982). The asperity model and the nature of large subduction
601 zone earthquakes.

602 Lay, T., & Kanamori, H. (1981). An asperity model of large earthquake sequences.

603 Li, Y., Doll Jr, C., & Toksöz, M. N. (1995). Source characterization and fault plane
604 determination for MbLg= 1.2 to 4.4 earthquakes in the Charlevoix Seismic Zone, Quebec,
605 Canada. *Bulletin of the Seismological Society of America*, *85*(6), 1604-1621.

606 Lin, Y. Y., & Lapusta, N. (2018). Microseismicity simulated on asperity-like fault patches: On
607 scaling of seismic moment with duration and seismological estimates of stress drops.
608 *Geophysical Research Letters*, *45*(16), 8145-8155.

609 Liu, M., Huang, Y., & Ritsema, J. (2020). Stress Drop Variation of Deep-Focus Earthquakes
610 Based on Empirical Green's Functions. *Geophysical Research Letters*, *47*(9), e2019GL086055.

611 Luco, J. E. (1985). On strong ground motion estimates based on models of the radiated spectrum.
612 *Bulletin of the Seismological Society of America*, *75*(3), 641-649.

613 Madariaga, R. (1976). Dynamics of an expanding circular fault. *Bulletin of the Seismological*
614 *Society of America*, *66*(3), 639-666.

615 Noda, H., Lapusta, N., & Kanamori, H. (2013). Comparison of average stress drop measures for
616 ruptures with heterogeneous stress change and implications for earthquake physics. *Geophysical*
617 *Journal International*, *193*(3), 1691-1712.

618 Oth, A. (2013). On the characteristics of earthquake stress release variations in Japan. *Earth and*
619 *Planetary Science Letters*, *377*, 132-141.

620 Papageorgiou, A. S., & Aki, K. (1983). A specific barrier model for the quantitative description
621 of inhomogeneous faulting and the prediction of strong ground motion. I. Description of the
622 model. *Bulletin of the Seismological Society of America*, *73*(3), 693-722.

623 Prieto, G. A., Froment, B., Yu, C., Poli, P., & Abercrombie, R. (2017). Earthquake rupture below
624 the brittle-ductile transition in continental lithospheric mantle. *Science Advances*, *3*(3),
625 e1602642.

626 Purvance, M. D., & Anderson, J. G. (2003). A comprehensive study of the observed spectral
627 decay in strong-motion accelerations recorded in Guerrero, Mexico. *Bulletin of the Seismological*
628 *Society of America*, *93*(2), 600-611.

629 Ruhl, C. J., Abercrombie, R. E., & Smith, K. D. (2017). Spatiotemporal variation of stress drop
630 during the 2008 Mogul, Nevada, earthquake swarm. *Journal of Geophysical Research: Solid*
631 *Earth*, *122*(10), 8163-8180.

632 Sato, T., & Hirasawa, T. (1973). Body wave spectra from propagating shear cracks. *Journal of*
633 *Physics of the Earth*, *21*(4), 415-431.

634 Shearer, P. M., Prieto, G. A., & Hauksson, E. (2006). Comprehensive analysis of earthquake
635 source spectra in southern California. *Journal of Geophysical Research: Solid Earth*, *111*(B6).

636 Shearer, P. M., Abercrombie, R. E., Trugman, D. T., & Wang, W. (2019). Comparing EGF
637 methods for estimating corner frequency and stress drop from P wave spectra. *Journal of*
638 *Geophysical Research: Solid Earth*, *124*(4), 3966-3986.

639 Sotiriadis, D., Margaris, B., Klimis, N., & Sextos, A. (2021). Implications of high-frequency
640 decay parameter,"κ-kappa", in the estimation of kinematic soil-structure interaction effects. *Soil*
641 *Dynamics and Earthquake Engineering*, *144*, 106665.

642 Trugman, D. T., Dougherty, S. L., Cochran, E. S., & Shearer, P. M. (2017). Source spectral
643 properties of small to moderate earthquakes in southern Kansas. *Journal of Geophysical*
644 *Research: Solid Earth*, *122*(10), 8021-8034.

645 Uchide, T., & Imanishi, K. (2016). Small earthquakes deviate from the omega-square model as
646 revealed by multiple spectral ratio analysis. *Bulletin of the Seismological Society of America*,
647 *106*(3), 1357-1363.

648 Ulrich, T., Gabriel, A. A., Ampuero, J. P., & Xu, W. (2019). Dynamic viability of the 2016 Mw
649 7.8 Kaikōura earthquake cascade on weak crustal faults. *Nature communications*, *10*(1), 1-16.

650 Vallée, M. (2013). Source time function properties indicate a strain drop independent of
651 earthquake depth and magnitude. *Nature communications*, *4*(1), 1-6.

652 Vallée, M., & Douet, V. (2016). A new database of source time functions (STFs) extracted from
653 the SCARDEC method. *Physics of the Earth and Planetary Interiors*, *257*, 149-157.

654 Wang, E., Rubin, A. M., & Ampuero, J. P. (2014). Compound earthquakes on a bimaterial
655 interface and implications for rupture mechanics. *Geophysical Journal International*, *197*(2),
656 1138-1153.

657 Wang, Y., & Day, S. M. (2017). Seismic source spectral properties of crack-like and pulse-like
658 modes of dynamic rupture. *Journal of Geophysical Research: Solid Earth, 122*(8), 6657-6684.

659 Wu, Q., Chapman, M., & Chen, X. (2018). Stress-drop variations of induced earthquakes in
660 Oklahoma. *Bulletin of the Seismological Society of America, 108*(3A), 1107-1123.

661 Ye, L., Lay, T., Kanamori, H., & Rivera, L. (2016). Rupture characteristics of major and great
662 (Mw≥ 7.0) megathrust earthquakes from 1990 to 2015: 1. Source parameter scaling
663 relationships. *Journal of Geophysical Research: Solid Earth*, *121*(2), 826-844.

664 Yin, J., Li, Z., & Denolle, M. A. (2021). Source time function clustering reveals patterns in
665 earthquake dynamics. *Seismological Society of America, 92*(4), 2343-2353.

666 Yu, H., Harrington, R. M., Kao, H., Liu, Y., Abercrombie, R. E., & Wang, B. (2020). Well
667 proximity governing stress drop variation and seismic attenuation associated with hydraulic
668 fracturing induced earthquakes. *Journal of Geophysical Research: Solid Earth*, *125*(9),
669 e2020JB020103.

670